

Positioning Annihilation Photon Interactions in a Thin LSO Crystal Sheet With a Position-Sensitive Avalanche Photodiode

Angela M. K. Foudray, *Student Member, IEEE*, Frezghi Habte, *Member, IEEE*, Craig S. Levin, *Member, IEEE*, and Peter D. Olcott, *Member, IEEE*

Abstract—Using scintillation crystal sheets instead of discrete crystal arrays in high-resolution PET has the immediate advantage of reduced complexity as well as a potential for increased sensitivity. In order to evaluate the positioning capability of a position sensitive avalanche photodiode (PSAPD) using a sheet Lutetium Oxyorthosilicate (LSO) crystal scintillator, we studied the dependence of detected event position versus the known source position. In particular, we studied positioning in a continuous 8 mm \times 8 mm LSO sheet coupled to a PSAPD with an 8 mm \times 8 mm active area experimentally, studied optical transport in the sheet crystal with Monte Carlo simulation, and used two positioning methods to evaluate PSAPD pincushioning effects. Both collimated ^{57}Co 122 keV and coincidence-triggered ^{22}Na 511 keV sources were used in the experiments performed. We analyze the energy resolution, sensitivity, photopeak position and spatial resolution as a function of source position. An average point spread function (PSF) resolution of 2.86 and 1.12 mm FWHM for ^{57}Co and ^{22}Na respectively was observed. Within 1.2 mm from the edge of the LSO sheet, the average photopeak position change was 5%. Simulations using annihilation photon interactions from GATE and scintillation photon transport from DETECT2000, as well as utilizing a pincushion-reduction positioning algorithm, have confirmed that the positioning and energy response observed experimentally at the edge of the crystal is due to optical transport near those edges.

Index Terms—Continuous crystal, DETECT2000, GATE, LSO, Monte Carlo, pincushion, sheet crystal.

I. INTRODUCTION

WE are developing a high-sensitivity, high-resolution small animal positron emission tomography (PET) system for studying the kinetics and mechanisms of human disease in small laboratory animal models. Most high-resolution imaging systems in use and in development are incorporating increasingly smaller pixellated scintillation crystals to try to improve system resolution [1], [2]. In order to increase the detection efficiency of the annihilation photons, the crystals are made long in the direction of the incoming photons. In standard PET detector designs, the photodetector is coupled to

Manuscript received November 15, 2004; revised March 30, 2006. This work was supported in part by NIH-NIBIB Grant R33 EB003283.

A. M. K. Foudray is with the Department of Physics, University of California-San Diego, La Jolla, CA 92037 USA and also with the Department of Radiology, the Molecular Imaging Program, Stanford University, Stanford, CA 94305 USA (e-mail: afoudray@stanford.edu).

F. Habte, C. S. Levin, and P. D. Olcott, are with the Department of Radiology and the Molecular Imaging Program, Stanford University, Palo Alto, CA 94305 USA (e-mail: fhabte@stanford.edu; pdo@stanford.edu; cslevin@stanford.edu).

Digital Object Identifier 10.1109/TNS.2006.877178

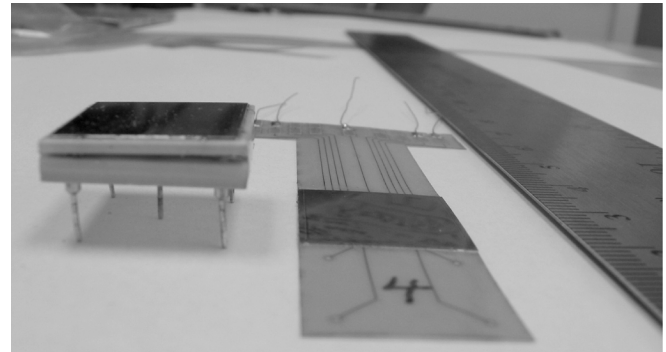


Fig. 1. Left: the studied prototype PSAPD, center: the thin PSAPD to be used in system construction.

the thin crystals on the side with the smallest cross-sectional area, giving them an aspect ratio that does not promote optimal light output [3], [4]. This results in a compromise between system resolution, light output (effectively energy resolution), and sensitivity [5]–[8].

Traditionally, PET detectors are made using scintillation crystals coupled to photomultiplier tubes (PMTs). Both segmented arrays, as well as continuous scintillation crystals, have been coupled to PMTs and position-sensitive PMTs to achieve high detector spatial resolution. For example, in the work by Cherry *et al.* [9], continuous crystals are coupled to an array of photomultiplier tubes to determine continuous positioning. PMTs, however, are large and resulting system configurations compromise either system solid-angle coverage or crystal packing fraction. There are definite advantages to this technology including that they are well characterized and relatively low in cost.

Recently developed detectors such as very thin position-sensitive avalanche photodiodes (PSAPDs) and cadmium zinc telluride (CZT) devices allow a very compact detector system, including photodetectors and the necessary electronics for signal acquisition. The thin PSAPD allows more advantageous scintillator coupling geometries and detector orientations, which significantly improve the sensitivity, energy resolution and spatial resolution (Fig. 1). With such small detectors, the packing fraction does not change significantly for different detector orientations. Crystals can then be coupled so that the aspect ratio is high (the PSAPD surface normal is perpendicular to the incoming photon direction), without reducing intrinsic sensitivity.

A pixellated crystal design facilitates spatial linearity across the entire face of the position-sensitive detector. If the photodetector has a higher intrinsic spatial resolution, the use of a continuous scintillator might provide superior spatial resolution to a discrete crystal design. A continuous scintillator also reduces manufacturing complexity and increases mechanical robustness of the detector system.

II. EXPERIMENTAL STUDY

A. Common Setup

We characterized a PSAPD developed by RMD, Inc. with an active region of 8 mm × 8 mm (Fig. 1, left) [2]. An 8 mm × 8 mm × 1 mm LSO continuous crystal is coupled to the PSAPD with silicon optical grease (~10 μm thick) and seven layers of Teflon were wrapped around the crystal to provide a reflector along the array surfaces not in contact with the PSAPD. A LabView-controlled, motorized, National Aperture MM-4M-EX-140 microstage was used to automate and accurately control the positioning steps across the detector. ⁵⁷Co (122 keV gamma) and ²²Na (511 keV annihilation photons) point sources were used to study the point spread function and spatial linearity of the PSAPD.

B. ²²Na Setup

The highly energetic 511-keV photons from the 10 μCi ²²Na point source were electronically collimated using a coincidence setup which was constructed using a Hamamatsu H3164 photomultiplier tube (PMT) that was coupled to a Teflon-wrapped 5 mm × 5 mm × 10 mm LSO crystal with silicone optical grease [see Fig. 2(a)]. The LSO-PMT detector was mechanically coupled to the source at a distance of 190 mm and moved with the microstage in 160 μm steps. The source-to-PSAPD distance was kept at a constant 1.5 mm. The geometry of the setup resulted in a ~540 μm spot size projected onto the face of the PSAPD. The coincidence circuit comprised Fast Filter Amplifiers, Constant Fraction Discriminators, a TAC/SCA, and Gate and Delay Generator NIM modules to trigger the four-channel PSAPD event acquisition.

C. ⁵⁷Co Setup

The ⁵⁷Co source was collimated using a 30 mm × 30 mm block of lead with a 500 μm hole [Fig. 2(b)]. The geometry of the setup resulted in a ~560 μm spot size on the face of the PSAPD. The four anode signals were acquired and processed in the same manner as the ²²Na setup — one spectrum amplifier and one delay amplifier per anode out to an acquisition board. The events were triggered by the signal from the common electrode (see Fig. 3).

III. POSITIONING

A. Methods

Due to the nonlinear nature of the charge distribution process over the face of the PSAPD detector, the calculated position

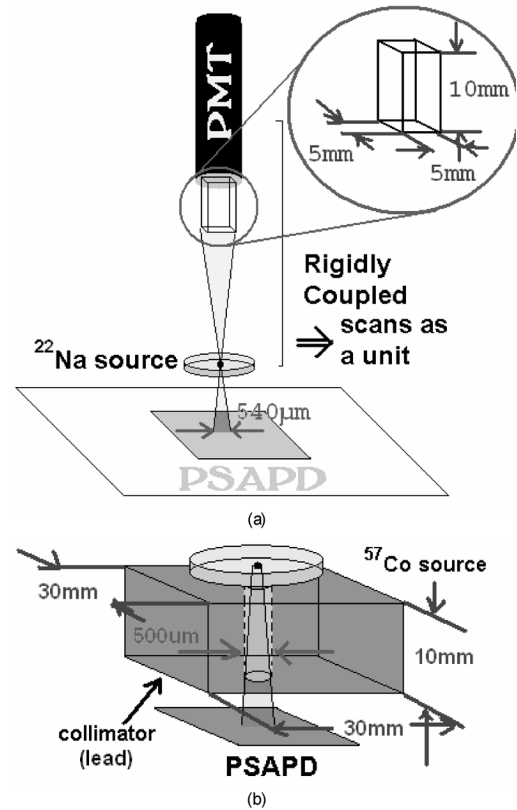


Fig. 2. The acquisition setup for (a) coincidence-collimated ²²Na annihilation photon detection with spot size ~500 μm and (b) lead collimated ⁵⁷Co gamma photon detection with spot size ~500 μm.

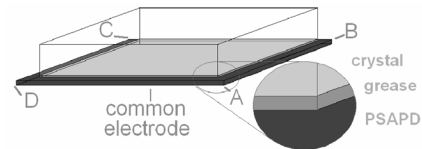


Fig. 3. A cartoon depicting anode positions used in (1) and (2), and layers of material used in all experiments and simulations.

map suffers from pincushion distortion when using traditional position calculation methods [10]. In order to help study the effect of pin cushioning, positions were calculated from the four digitized PSAPD channels using a new method as well as the traditional method of Anger-type logic.

The first positioning method uses an algorithm developed by Zhang *et al.* [11] to reduce the effect of nonlinear positioning of the PSAPD. The position is calculated from the four digitized voltages from only the opposing corner anodes of the PSAPD (Fig. 3) using the following equations:

$$x' = \frac{B - D}{B + D} \quad (1)$$

$$y' = \frac{C - A}{C + A} \quad (2)$$

$$x = y' \cos(\pi/4) - x' \sin(\pi/4) \quad (3)$$

$$y = x' \cos(\pi/4) + y' \sin(\pi/4) \quad (4)$$

Using the traditional position-determining method, position is calculated from the four digitized voltages from all four corner anodes of the PSAPD, using the following [10]:

$$x = \frac{(A + B) - (C + D)}{A + B + C + D} \quad (5)$$

$$y = \frac{(C + B) - (A + D)}{A + B + C + D}. \quad (6)$$

The range for A, B, C, and D is [0,5] V; the range for x and y using method 1 or 2 is [-1, 1] (unitless). The energy for each event, using either method, is calculated from the sum $A + B + C + D$ and has a range of [0, 20] V. The units of position and therefore the point spread function full width at half maximum (psfFWHM), as well as the average energy, are all reported in the range of the positioned events for conciseness: [-0.3, 0.3]. The dynamic range is compressed due to light spread across the whole face of the PSAPD [2] for every event.

B. Method Assessment

To understand characteristics of positioning using these two methods, the shape of the calculated PSF was modeled as an ellipse and its position dependent size, orientation, and calculated location was quantified in standard image processing methods using the second moment of the image. The angle that the major axis makes with the x axis of the image is calculated in the following manner [12] shown in (7)–(8) at the bottom of the page.

The variables that are included for characterizing the resulting calculated PSF ellipse are: angle θ , major axis “a,” and minor axis “b,” which were measured across the face of the detector for both positioning methods.

IV. MONTE CARLO STUDY

In the following, Monte Carlo simulations, only optical transport in the continuous LSO crystal is modeled in the positioning of events. To compare the experimental results with a system that does not involve positioning affects due to the PSAPD, we utilized two standard simulation packages to model both the high energy and the light photon interactions in the LSO scintillation crystal. The interaction mechanisms of the high-energy annihilation photons were simulated with GATE [13], the medical imaging Monte Carlo add-on package to the high energy physics GEANT4 software. The subsequent scintillation photon transport and interactions were carried out using the DETECT2000 package [14].

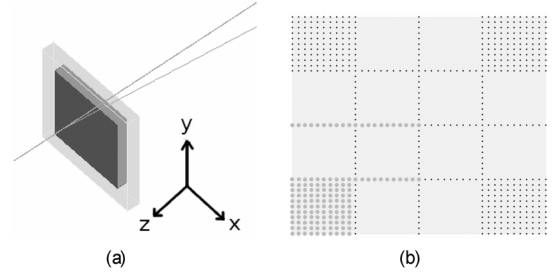


Fig. 4. (a) A screen shot during GATE simulation. Dark gray parallel-piped: LSO crystal, light gray parallel-piped: volume of module, gray lines: high-energy photon trajectories, left of dark gray LSO crystal: the origin of the source, right: the transmitted photons. (b) The source positions that were simulated are represented by the large gray dots. The behavior at the small dark gray positions is known by symmetry of the PSAPD device. The light gray area represents the active area of the PSAPD.

A. GATE

To simulate similar conditions as seen in the ^{22}Na experimental coincidence study, GATE was used to obtain Compton scatter, Photoelectric and characteristic X-ray interaction positions in the LSO scintillation crystal. A 20- μm radius sphere containing 511-keV activity was placed 5 mm from the surface of an 8 mm \times 8 mm \times 1 mm single LSO crystal, emitting normal to the surface of the crystal [Fig. 4(a)]. Each interaction with the crystal is recorded by GATE into a “hits” file, which gives specific information including the energy, three-dimensional (3-D) position, and annihilation event number. In order to probe the location-dependent response and light spread, the source sphere was stepped at 200 μm increments at the locations on the face of the detector shown in Fig. 4(b) as dark gray dots. The position, energy and event number were passed, for each “hits” interaction to DETECT2000, which simulated optical transport within the crystal.

B. DETECT2000

The interactions determined by GATE were modeled as a point process, i.e., the scintillation photons modeled by DETECT2000 for a particular GATE interaction (“hit”) were all given the same initial location determined in the “hits” file. DETECT2000 requires for input a location and number of photons to generate and outputs, for each scintillation photon, a location on the photodetector surface. The energy given in the GATE “hits” file was converted to a number of photons to generate for the DETECT2000 step assuming an average LSO conversion efficiency of 25 photons per keV. Generating a constant

$$M_{xx} = \frac{\sum x^2}{\sum x}, M_{yy} = \frac{\sum y^2}{\sum y}, M_{xy} = \frac{\sum xy}{\sum x} \quad (7)$$

$$\theta = a \tan\left(\frac{M_{yy} - M_{xx} + \sqrt{(M_{yy} - M_{xx})^2 + 4M_{xy}^2}}{2M_{xy}}\right). \quad (8)$$

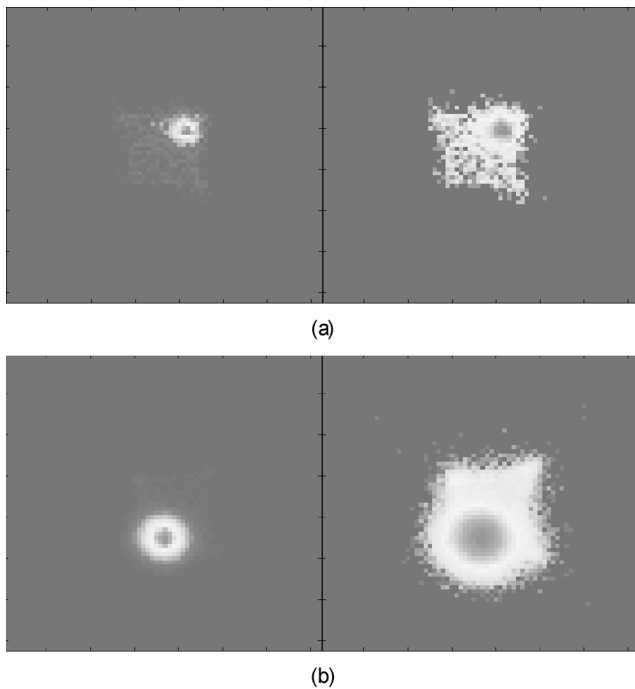


Fig. 5. For a single source position, (left) the measured PSF and (right) the log of the histogram values (enhance the visualization of the dynamic range). All images use the traditional positioning algorithm (5) and (6). (a) Point spread function for ^{22}Na . (b) Point spread function for ^{57}Co .

number of photons per keV for each interaction limits the factors affecting energy resolution of the detector to optical transport effects: absorption, scatter, transmission, reflection, as well as material index of refraction.

The two materials simulated are shown in Fig. 3: an $8\text{ mm} \times 8\text{ mm} \times 1\text{ mm}$ LSO crystal, with index of refraction 1.82, and a $10\text{ }\mu\text{m}$ thick optical grease layer with the same cross section and an index of refraction of 1.465. The surface finish on the five faces of the scintillation crystal not in contact with the optical grease were considered ground, and the sixth connecting face, polished. These surface definitions were mirrored in the grease layer, except for the side considered in contact with the PSAPD, which was defined as the “detect” layer. Scintillation photons that come in contact with this detect layer are considered detected and the position and location are automatically written out. The centroid of these locations were calculated in postprocessing and averaged to compare to the results obtained in experiment.

V. RESULTS

A. Experimental Results

Fig. 5 uses the traditional positioning method and shows the measured PSF at a position near the right edge using the ^{22}Na coincidence setup [see Fig. 5(a)] and a position to the left of center for the ^{57}Co collimation setup [see Fig. 5(b)]. The log of the histogrammed counts shown in the left-hand side of the image are displayed on the right-hand side to show the relative size of the spread of events with respect to the size of the area of dynamic range.

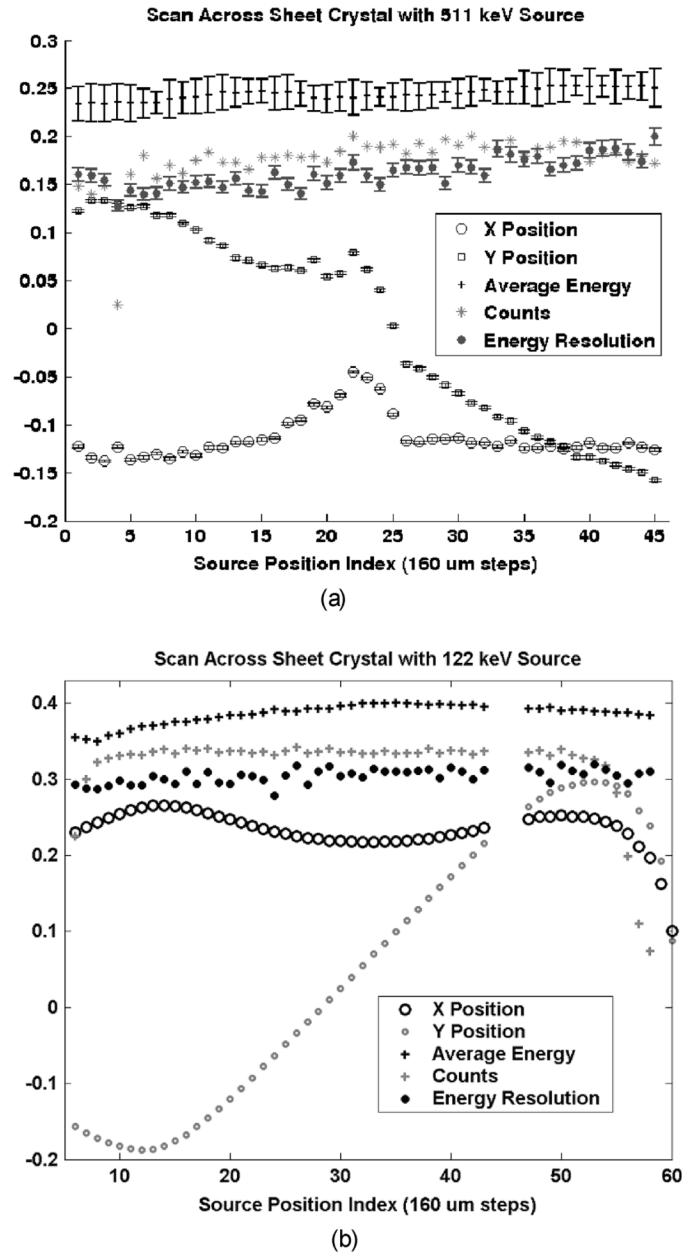


Fig. 6. Position, photopeak location, counts, and energy resolution for both (a) ^{22}Na and (b) ^{57}Co . All quantities are in volts, except for counts. Energy resolution, photopeak location, and counts are scaled to visualize all data in one graph. Error bars for photopeak location, counts, and energy resolution are the standard deviation of three measurements. Position error is calculated using bootstrap. In (b), the error bars are smaller than the data point symbol size.

Data were gathered for 2000 s (33 min) at each location using the ^{22}Na setup and for 120 s for the ^{57}Co . Although the acquisition times for the ^{22}Na setup were much longer, the number of events is much lower because electronic coincidence was used for collimation (~ 1000 events after energy gating at full width fifth max for ^{22}Na , versus $>30\,000$ for the collimated ^{57}Co source). The centroid of the positions of the events for a particular source location was calculated and plotted along with the number of counts, average energy, and energy resolution (Fig. 6). During the portion of the acquisition of the ^{22}Na coincidence data when the source was directly over the center of the crystal, we recorded a large deviation in spatial linearity for

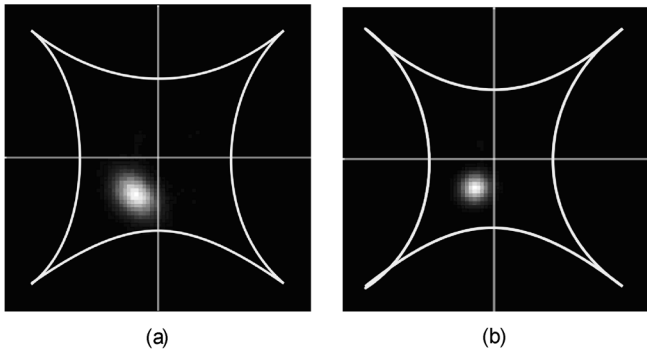


Fig. 7. The 2-D histograms for a ^{57}Co source, location index 15 (1.28 mm from the left edge), using both positioning methods. The white pin-cushioned outlines show the range of positioning on the PSAPD for each method. Note: the range is larger for positioning method 1 (see Fig. 8). The light gray cross-hair lines show the center of the PSAPD. (a) Point spread function for method 1 [(1)–(4)]. (b) Point spread function for method 2 [(5)(6)].

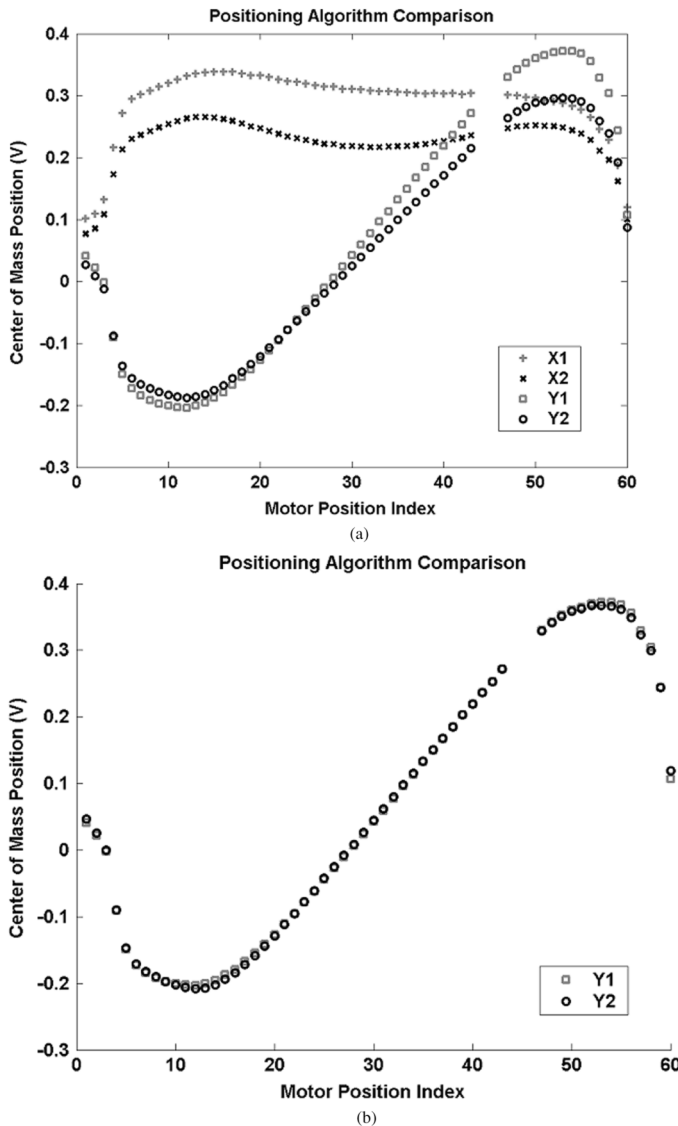


Fig. 8. (a) Centroid positions of the point spread function using the positioning algorithm method 1 (X1, Y1) and method 2 (X2, Y2). (b) Y2 scaled to Y1.

both the direction in which the source was moving “x” as well as perpendicular to it “y” [see Fig. 6(a)]. We believe this anomaly is due to a portion of the moving PMT-source structure becoming

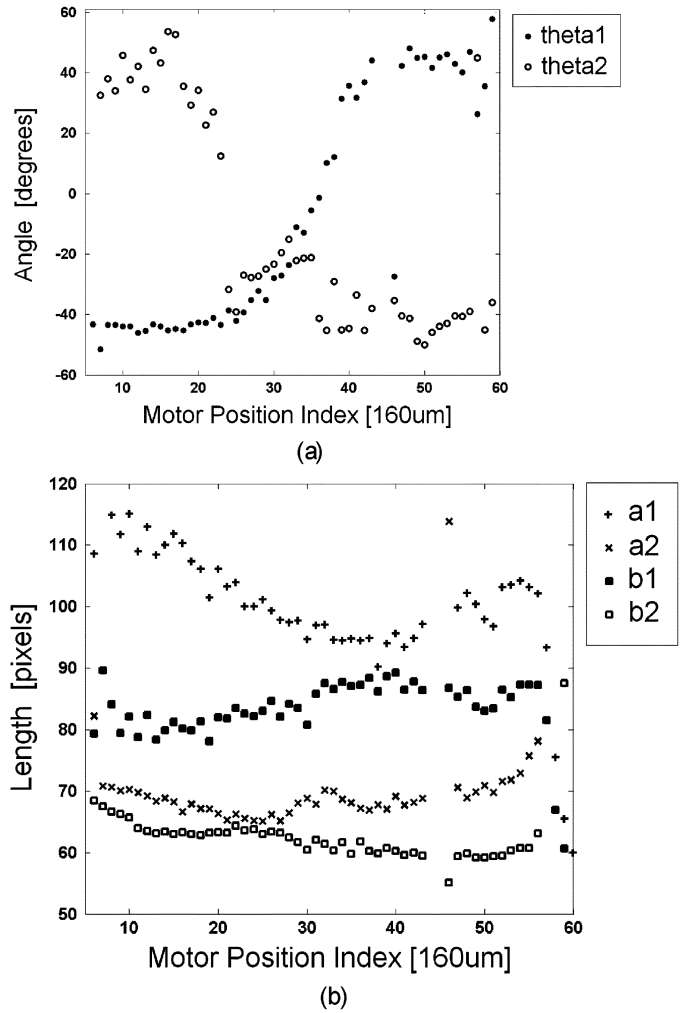


Fig. 9. Using positioning methods 1 and 2, the shape of the PSF was modeled as an ellipse. (a) The angle between the major axis of the PSF ellipse and the x axis of the image is plotted for both methods across the face of the detector. (b) The FWHM of the ellipse along the major axis “a” and minor axis “b” is plotted for both methods across the face of the detector.

impeded during a few millimeters of its motion. The linearity of the calculated position versus known source position resumed after the anomaly. There was a short period during the acquisition using the ^{57}Co source [see Fig. 6(b)] that a scheduled software process took priority over acquisition and resulted in three data points being lost.

Note also that the average photopeak position does not remain constant at the edge of the detector, and potentially provides a fifth positioning parameter to resolve positioning difficulties at the edge. The average raw FWHM energy resolution for ^{57}Co was $24.45\% \pm 0.2\%$ at 122 keV and $17.33\% \pm 1.06\%$ at 511 keV for ^{22}Na within 2 mm of the center. Within 2 mm of the edges, the uncorrected FWHM energy resolution for ^{57}Co was $24.92\% \pm 0.2\%$ at 122 keV and $15.24\% \pm 1.18\%$ at 511 keV for ^{22}Na . The error is the standard deviation of all the measurements for a group of data.

The measured psfFWHM, using the traditional positioning method (method 2), averaged 2.9 mm for ^{57}Co and 1.23 mm for ^{22}Na . Deconvolving the finite size of the source, $500 \mu\text{m}$ was used as a conservative value for both the ^{57}Co

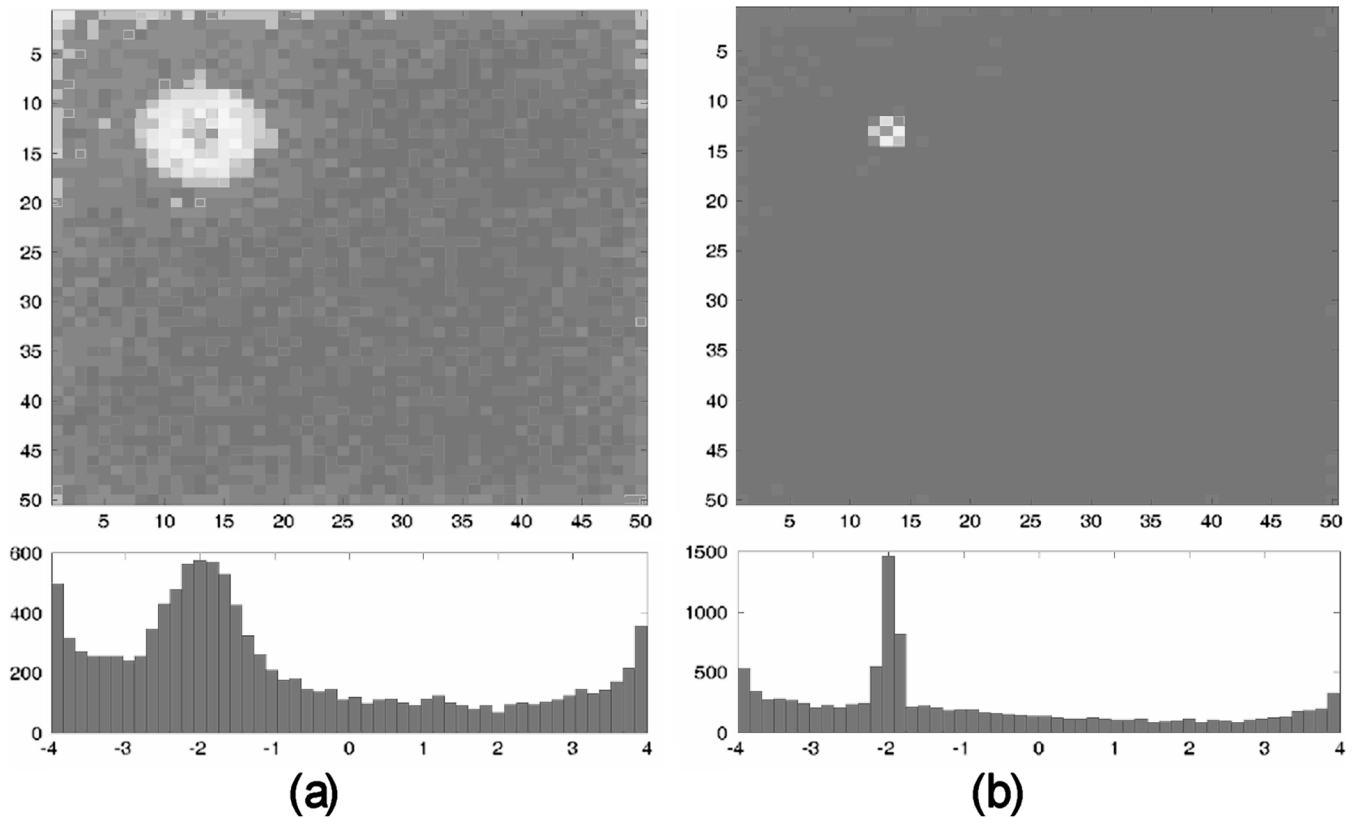


Fig. 10. 2- and 1-D histograms of the individual scintillation photons from one “hits” interaction which originated (a) $z = 0.63$ mm. (b) $z = 0.16$ mm from the photodetector surface inside the crystal. Both events have the same energy and (x,y) position within the crystal (coordinate system defined in Fig. 4).

and ^{22}Na case. Using a first approximation $\sqrt{(\text{meas. psf-FWHM})^2 - (500 \mu\text{m})^2}$ gives 2.86 mm FWHM for ^{57}Co and 1.12 mm FWHM for ^{22}Na . The positioning linearity for the central 6 mm has an R^2 -value of 0.965 for ^{22}Na (not including the points taken during impeded source motion) and 0.9995 for ^{57}Co .

B. Positioning Method Results

Fig. 7 shows the 2-D histogram of photon interaction events in the sheet crystal using both positioning algorithms and a ^{57}Co source. The source is at position index 15 or 1.28 mm from the left edge of the crystal. Both images have the same dynamic range: $[-1.5, 1.5]$, but notice the dynamic range difference (location of the center of the spot in the image) and the difference in spot shape and distribution.

Looking at the centroid locations in x and y , using both positioning methods, as a function of source position index (Fig. 8), we observe an increase in dynamic range when using positioning method one [see Fig. 8(a)]. When rescaling and translating the centroid positions calculated using positioning method two to cover the same range as positioning method one, the centroid locations are very similar [see Fig. 8(b)]. Therefore, the positioning algorithm which reduces the pincushion distortion does not affect the positioning degeneracy near the edges of the detector.

Fig. 9 shows differences in properties of the shape of the PSF for both positioning methods. Modeling the area of the PSF as

an ellipse, the major axis length “ a ” and minor axis length “ b ” were calculated from the second moment of the shape of the PSF and plotted in Fig. 9. Looking at the major and minor axes lengths, the first positioning algorithm produces a PSF with a larger FWHM in both directions. Note also the elongation of the PSF at a single position [shown in Fig. 7(a)] using positioning method 1 as opposed to the relatively circular shape of the PSF when using positioning method 2 [see Fig. 7(b)]. The angle that the major axis makes with the x axis is also plotted in Fig. 9. Although both positioning methods happen to have the similar ranges of orientation angles, the degree to which the second positioning algorithm is noncircular is much reduced. This can be seen by the smaller difference between the major and minor axis lengths for the second positioning algorithm [Fig. 7(a)].

C. Simulation Results

Fig. 10 shows the effect of interaction depth measured from the surface of the crystal to the detector, of the annihilation photon interaction within one crystal on light spread within that crystal. Not to be confused with Fig. 5, Fig. 10 shows histograms of the locations of the individual scintillation photons detected from one annihilation event. The centroid of the positions shown in Fig. 10 makes up one event in the histogram of Fig. 5.

The energy surface at the corner of the dcrysal sheet [the 10×10 location patch shown in Fig. 4(b)] is shown in Fig. 11. The calculated position plotted [see Fig. 12(a)] is the mean of the centroids of the photons from an event over the entire crystal. The average energy (number of scintillation photons) is shown

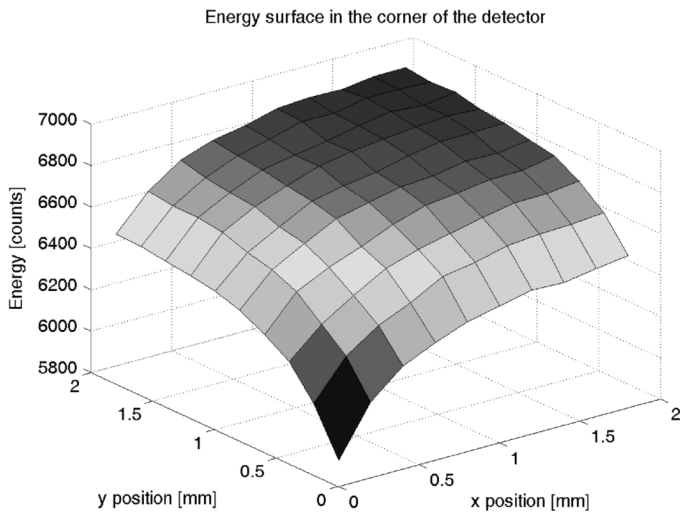


Fig. 11. Average energy at locations in the corner of the crystal sheet.

in Fig. 12(b). Averages were calculated from 300 GATE simulations for simulated events and over the interactions detected for the experimental events.

The PSAPD resistive surface was not modeled to simulate pin-cushion effects. Pin-cushioning adds nonlinear distortions in the position estimates [10]. There is a larger region over which the experimentally calculated position for the 122 keV ^{57}Co data is nonlinear possibly due to more interactions are happening closer to the top of the crystal, i.e., farther from the detector surface.

VI. CONCLUSION

The experimental and simulated results agree quite well — both show that the calculated positions from events whose centroid are within 1.2 mm from the edge of the sheet crystal are degenerate. A positioning method that reduces the pin-cushion distortion was employed to reduce nonlinearities in positioning on the surface of the PSAPD, but did not succeed in reducing the region of positioning degeneracy. Therefore, the degeneracy seems to be due to the edge effects within the scintillation crystal — a sizable portion of the scintillation photons reflect off the surface of the sides of the crystal. Because of these reflections, some photons are lost through transmission and absorption, which changes the average energy of events positioned at the edge as compared to events at the center of the detector. The percentage change in energy within 1.2 mm from the edge is about 5%. Thus, in order to resolve positions near the edge using a single sheet crystal (that is the same size as the active area of the detector), we would need a detector with better than 5% energy resolution. However, the energy resolution of our characterized PSAPD with this scintillator is 10%–12%.

To compare these results to those of segmented crystals of the same scintillator coupled the same photodetector, we can look at a summary of the position resolution experiments performed by Zhang, *et al.* [11] using $1 \times 1 \times 3 \text{ mm}^3$ segmented crystals packed in an $8 \times 3 (8 \text{ mm} \times 9 \text{ mm})$ array coupled to the PSAPD detector. The average energy resolution at 511 keV was comparable: 12.61% and the average deconvolved FWHM of the PSF

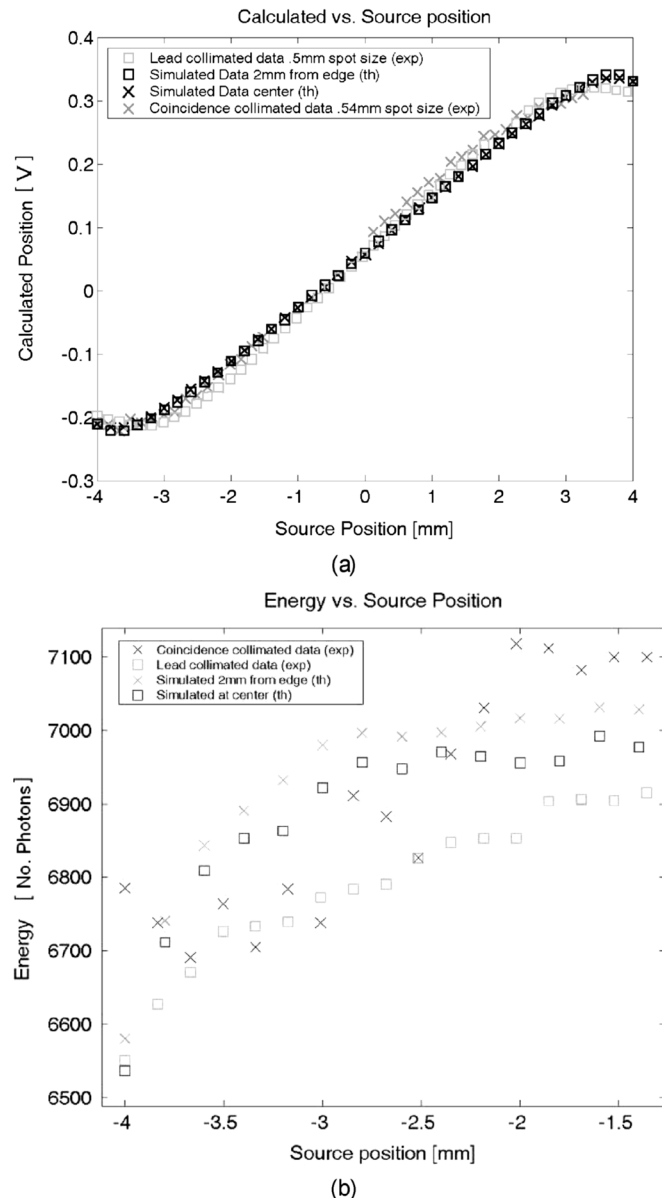


Fig. 12. Comparison of experimental (exp) and simulated (th) calculated (a) position and (b) energy versus source position. The experimental data are the ^{22}Na and ^{57}Co data plotted in Fig. 6. The simulated source locations are seen in Fig. 4(b) as dark gray dots.

was 1.09 mm, also comparable to the results found in this study. On the same photodetector device with the segmented crystals, the paper mentions our difficulty in resolving the array crystals near the edge — this is where we observed degeneracy in the sheet crystal. This difficulty was greatly reduced when studying the spatial resolution capabilities of the new thin photodetector introduced in the paper.

Further efforts to utilize all the information collected from the four anode channels to reduce degeneracy might involve maximum-likelihood position estimation algorithms. Future experiments will include positioning accuracy of events near the edge of the PSAPD active area when the continuous crystal is larger than the PSAPD active area. The increased sensitivity [11], [15] of these larger crystals and potential decrease in crystal edge-effect positioning problems suggests further study.

ACKNOWLEDGMENT

The authors would like to acknowledge R. Farrell, M. McClish, M. Squillante, and K. Shah at RMD, Inc., for their ideas and support.

REFERENCES

- [1] Y. C. Tai, A. F. Chatziioannou, M. Dahlbom, and S. R. Cherry, "System design for a 1 mm³ resolution animal pet scanner: Micropet ii," *IEEE Nucl. Sci. Symp. Conf. Rec.*, vol. 3, pp. 51–52, 2000.
- [2] C. S. Levin, A. M. K. Foudray, P. D. Olcott, and F. Habte, "Investigation of position sensitive avalanche photodiodes for a new high resolution pet detector design," *IEEE Trans. Nucl. Sci.*, vol. 51, no. 3, pp. 805–810, Jun. 2004.
- [3] C. S. Levin, "Design of a high-resolution and high-sensitivity scintillation crystal array for pet with nearly complete light collection," *IEEE Trans. Nucl. Sci.*, vol. 49, no. 5, pt. 1, pp. 2236–2243, Oct. 2002.
- [4] C. S. Levin, F. Habte, and A. M. K. Foudray, "Methods to extract more light from minute scintillation crystals used in an ultra-high resolution positron emission tomography detector," *Nucl. Instrum. Methods Phys. Res. Sect. A*, vol. 527, no. 1–2, pp. 35–40, Jul. 2004.
- [5] A. F. Chatziioannou, S. R. Cherry, Y. P. Shao, R. W. Silverman, K. Meadors, T. H. Farquhar, M. P. Amd, and M. E. Phelps, "Performance evaluation of micropet: A high-resolution lutetium oxyorthosilicate pet scanner for animal imaging," *J. Nucl. Med.*, vol. 40, no. 7, pp. 1164–1175, Jul. 1999.
- [6] A. P. Jeavons, R. A. Chandler, and C. A. Dettmar, "A 3D hidac-pet camera with sub-millimetre resolution for imaging small animals," *IEEE Trans. Nucl. Sci.*, vol. 46, no. 3, pt. 2, pp. 468–473, Jun. 1999.
- [7] B. J. Pichler, B. K. Swann, J. Rochelle, R. E. Nutt, S. R. Cherry, and S. B. Siegel, "Lutetium oxyorthosilicate block detector readout by avalanche photodiode arrays for high resolution animal pet," *Phys. Med. Biol.*, vol. 49, no. 18, pp. 4305–4319, Sep. 2004.
- [8] J. Joung, R. S. Miyaoka, and T. K. Lewellen, "Cmice: A high resolution animal pet using continuous Iso with a statistics based positioning scheme," *Nucl. Instrum. Methods Phys. Res. Sect. A*, vol. 489, no. 1–3, pp. 584–598, Aug. 2002.
- [9] S. Cherry, S. Siegel, A. Ricci, L. Eriksson, E. Hoffman, and M. Phelps, "Development of position sensitive detectors for use in positron emission tomography of small laboratory animals," *Nucl. Instrum. Methods Phys. Res., Section A: Accelerators, Spectrometers, Detectors and Assoc. Equip.*, vol. 348, no. 2–3, pp. 613–617, Sep. 1, 1994.
- [10] K. S. Shah, R. Farrell, R. Grazioso, E. S. Harmon, and E. Karplus, "Position-sensitive avalanche photodiodes for gamma-ray imaging," *IEEE Trans. Nucl. Sci.*, vol. 49, no. 4, pt. 1, pp. 1687–1692, Aug. 2002.
- [11] J. Zhang, A. M. K. Foudray, P. D. Olcott, and C. S. Levin, "Performance characterization of a novel thin position-sensitive avalanche photodiode for a high resolution pet camera," in *IEEE Nucl. Sci. Symp. Med. Imag. Conf. Rec.*, 2005.
- [12] B. Jahne, *Digital Image Processing*, 5th ed. New York: Springer, 2001.
- [13] S. Jan, G. Santin, D. Strul, S. Staelens, K. Assie, D. Autret, S. Avner, R. Barbier, M. Bardies, P. M. Bloomfield, D. Brasse, V. Breton, P. Bruyndonckx, I. Buvat, A. F. Chatziioannou, Y. Choi, Y. H. Chung, C. Comtat, D. Donnarieix, L. Ferrer, S. J. Glick, C. J. Groiselle, D. Guez, P. F. Honore, S. K. Cavata, A. S. Kirov, V. Kohli, M. Koole, M. Krieguer, D. J. van der Laan, F. Lamare, G. Largeron, C. Lartizien, D. L. M. C. Maas, L. Maigne, F. Mayet, F. Melot, C. Merheb, E. Pennacchio, J. Perez, U. Pietrzyk, F. R. Rannou, M. Rey, D. R. Schaart, C. R. Schmidlein, L. Simon, T. Y. Song, J. M. Vieira, D. Visvikis, R. V. de Walle, E. Wieers, and C. Morel, "Gate: A simulation toolkit for pet and spect," *Phys. Med. Biol.*, vol. 49, no. 19, pp. 4543–4561, Oct. 2004.
- [14] F. Habte, P. D. Olcott, A. M. K. Foudray, C. S. Levin, J. Zhang, and G. Chinn, "Simulation and measurement of gamma ray and annihilation photon imaging detectors," *IEEE Trans. Nucl. Sci.*, submitted for publication.
- [15] A. M. K. Foudray, F. Habte, G. Chinn, J. Zhang, C. S. Levin, and P. D. Olcott, "Optimization of a pet breast imaging system comprised of position sensitive avalanche photodiodes utilizing monte carlo simulation," *Presented at the 2004 IEEE NSS-MIC Breast Cancer Workshop*, 2004.